PHYSICAL REVIEW E **74**, 011502 (2006)

Dynamics of ternary mixtures with photosensitive chemical reactions: Creating three-dimensionally ordered blends

Olga Kuksenok, Rui D. M. Travasso, and Anna C. Balazs
Chemical Engineering Department, University of Pittsburgh, Pittsburgh, Pennsylvania 15261, USA

(Received 31 January 2006; published 11 July 2006)

Using computer simulations, we establish an approach for creating defect-free, periodically ordered polymeric materials. The system involves *ABC* ternary mixtures where the *A* and *B* components undergo a reversible photochemical reaction. In addition, all three components are mutually immiscible and undergo phase separation. Through the simulations, we model the effects of illuminating a three-dimensional (3D) sample with spatially and temporally dependent light irradiation. Experimentally, this situation can be achieved by utilizing both a uniform background light and a spatially localized, higher intensity light, and then rastering a higher-intensity light over the 3D sample. We first focus on the case where the higher-intensity light is held stationary and focused in a distinct region within the system. The *C* component is seen to displace the *A* and *B* within this region and replicate the pattern formed by the higher-intensity light. In effect, one can write a pattern of *C* onto the *AB* binary system by focusing the higher-intensity light in the desired arrangement. We isolate the conditions that are necessary for producing clearly written patterns of *C* (i.e., for obtaining sharp interfaces between the *C* and *A*/*B* domains). We next consider the effect of rastering a higher-intensity light over this sample and find that this light "combs out" defects in the *AB* blend as it moves through the system. The resulting material displays a defect-free structure that encompasses both a periodic ordering of the *A* and *B* domains and a well-defined motif of *C*. In this manner, one can create hierarchically patterned materials that exhibit periodicity over two distinct length scales. The approach is fully reversible, noninvasive, and points to a novel means of patterning with homopolymers, which normally do not self-assemble into periodic structures.

DOI: 10.1103/PhysRevE.74.011502 PACS number(s): 64.75.+g, 64.60.Cn, 61.41.+e, 82.40.Ck

I. INTRODUCTION

There is a significant drive to harness self-assembling polymers in a variety of microelectronic devices; the fact that the materials are polymers reduces the cost of fabrication and the self-assembling aspect reduces the number of processing steps, which again reduces cost. However, there are a number of critical requirements that typically must be met before self-assembling polymers can be implemented in the production of electronic components. In particular, the following conditions must be satisfied: (i) the system should form hierarchical structures, with some domains being on the submicron or nanoscale scale, while other domains are on the micron scale, (ii) the material should be defect free on the cm to mm length scale, and (iii) it should be possible to form a wide variety of patterns. Researchers have addressed these issues, particularly items (ii) and (iii), by directing the self-organization of block copolymer films with an underlying patterned substrate [1,2]. In this manner, the systems exhibited nanoscale features and macroscopic order (with ordered regions that are $1\,\mathrm{cm}^2$ in size)[2]. In addition, the substrate could be patterned into nonregular shapes and the overlying copolymers or copolymer/homopolymer mixture could be made to replicate the underlying design [2].

In a recent study [3,4], we proposed an alternative approach that does not rely on self-assembling copolymers to address the issues listed above. In particular, we used a two dimensional computational model to demonstrate how photoinduced chemical reactions can be exploited to create long-range order in binary and ternary homopolymer films. The process is initiated by shining a spatially uniform light over a photosensitive *AB* binary homopolymer blend, which thereby undergoes both a reversible chemical reaction and phase separation. We then introduce a well-collimated, higher-intensity light source. Rastering this secondary light over the sample locally increases the reaction rate and causes formation of defect-free, spatially periodic structures. These binary structures resemble either the lamellar or hexagonal phases of microphase-separated diblock copolymers. We then add a nonreactive homopolymer *C*, which is immiscible with both *A* and *B*. We showed that this component migrates to regions that are illuminated by the secondary, higher intensity light, allowing us to effectively write a pattern of *C* onto the *AB* film. Rastering over the ternary blend with a collimated, high-intensity light now leads to hierarchically ordered patterns of *A*, *B* and *C*.

In addition to addressing items (ii) and (iii) above, the approach allows one to readily create a variety of hierarchical patterns, where some features are on the submicron size scale, while others domains on the micron scale. Furthermore, the resulting structures exhibit periodicity over multiple length scales. Since our approach involves homopolymers rather than block copolymers, it introduces a new way of creating ordered, periodic structures from these simpler systems. The findings point to a facile, nonintrusive process for manufacturing high-quality polymeric devices in a low-cost, efficient manner.

As noted above, our previous studies were focused on polymer films. Herein, we extend the approach to three dimensions and thereby examine how to form hierarchically ordered, defect-free materials in bulk binary and ternary systems.

As in the previous study, we begin by considering a binary *AB* blend that undergoes the following photoinduced reversible chemical reaction:

$$A \overset{\Gamma_+}{\underset{\Gamma_-}{\Leftrightarrow}} B, \tag{1}$$

where the parameters Γ_+ and Γ_- represent the forward and reverse reaction rate coefficients, respectively. In addition, A and B components undergo phase separation. There are a number of examples of reaction-induced phase separation in photosensitive systems. Blends of trans-stilbene labeled polystyrene and poly (vinyl methyl ether) (PSS/PVME) constitute one well-known example [5–7]. Upon irradiation, the stilbene moieties on the PSS chains undergo a reversible *trans-cis* photoisomerization. Once the reaction reaches a certain threshold, the mixture undergoes phase separation since the *cis*-labeled polystyrene and PVME are immiscible. Thus, a reversible chemical reaction and phase separation are taking place simultaneously within this binary blend. Other photosensitive pendent groups can also be used to yield a similar behavior [5–7].

An important feature of our model is that we assume that the above reaction rates coefficients can be controlled through an external light source, and consequently, the reaction rate coefficients vary in both space and time—i.e., $\Gamma \equiv \Gamma(r,t)$. In the corresponding experiments, this would mean, for example, that different regions of the sample would be exposed to light of different intensities and the intensity of the irradiating light would be altered with time [7]. We note that the behavior of binary mixtures that undergo phase separation and chemical reaction, as in Eq. (1), has been well studied (see, for example, [8–11]). In particular, it is well known that the morphologies in such mixtures resemble the morphologies observed in microphase-separated diblock copolymers [9,11]. There has also been significant progress in understanding the kinetics of ternary phase-separating mixtures in the absence of chemical reactions (see, for example, [12–18] and references therein). To date, however, the behavior of reactive ternary mixtures has received considerably less attention [19–23]. Researchers have examined diblock/homopolymer mixtures [24] that display structures similar to patterns described below (i. e., those in which the reaction rate coefficients are constant throughout the sample). Other than our previous studies [3,4], to the best of our knowledge, there have been no studies of phase-separating ternary mixtures undergoing the reaction in Eq. (1), where the reaction rate coefficients are varied in space and in time.

In what follows below, we first provide a description of our theoretical model. We then show how one can control the evolution of such systems by varying the reaction rate coefficients in a specified manner. Finally, we discuss our findings on the formation of defect-free structures in the bulk binary and ternary systems.

II. THE MODEL

As noted above, we investigate the structural evolution of ABC ternary mixtures, where the AB binary blend undergoes the photoinduced, reversible chemical reaction described by Eq. (1). In the following studies, we assume that the forward and reverse reaction coefficients are equal—i.e., $\Gamma_+ = \Gamma_- \equiv \Gamma$. The C component in the mixture is nonreactive; it is simply immiscible with both A and B. The volume fraction of each component is given by ρ_i, where $i = A, B, C$, and the mixture is assumed to be incompressible—i.e., $\Sigma_i \rho_i = 1$. To describe the concentration distributions in our system, we define two order parameters; the first-order parameter is the difference between the volume fractions of the A and B components, $\varphi = \rho_A - \rho_B$, and the second-order parameter is the volume fraction of the C component, $\psi = \rho_C$.

The evolution of the two order parameters is described by the following modified Cahn-Hilliard equations, where the equation for φ incorporates the appropriate reactive term [4,25]:

$$\frac{\partial \varphi}{\partial t} = M_\varphi \nabla^2 \mu_\varphi - 2\Gamma \varphi, \tag{2}$$

$$\frac{\partial \psi}{\partial t} = M_\psi \nabla^2 \mu_\psi. \tag{3}$$

Here, M_φ and M_ψ are the respective mobilities of the two order parameters and are taken to be constants. The respective chemical potentials μ_φ and μ_ψ are defined through the free energy functional $F(\varphi, \psi)$ as

$$\mu_\varphi = \frac{\delta F(\varphi,\psi)}{\delta \varphi}, \quad \mu_\psi = \frac{\delta F(\varphi,\psi)}{\delta \psi}. \tag{4}$$

The form of the free energy functional is taken to be [17]

$$F(\varphi,\psi) = \frac{1}{V}\int d\mathbf{r}[-a_{20}\varphi^2 + a_{40}\varphi^4 + a_{02}\psi^2 - a_{03}\psi^3 + a_{04}\psi^4 + a_{22}\varphi^2\psi^2 + \kappa_\varphi(\boldsymbol{\nabla}\varphi)^2 + \kappa_\psi(\boldsymbol{\nabla}\psi)^2]. \tag{5}$$

We determine the values of the coefficients a_{ij} in Eq. (5) by requiring the local free energy to have equal minima at $\varphi = \pm 1$; $\psi = 0$ [which corresponds to the pure $A(B)$ phase] and $\varphi = 0$; $\psi = 1$ (which corresponds to the pure C phase). Moreover, we require the free energy to be symmetric with respect to all three of the components. In particular, we choose [17]

$$a_{40} = 0.5a_{20}, \quad a_{02} = 3a_{20}, \quad a_{03} = 8a_{20}, \quad a_{04} = 4.5a_{20}, \quad a_{22} = 3a_{20}, \quad a_{20} = 0.5. \tag{6}$$

The two gradient terms in Eq. (5) are related to the interfacial tension γ_{ij} between the different components. Since we assume that $\gamma_{AC} = \gamma_{BC}$, these two gradient terms are sufficient to describe our system [i.e., there is no $\boldsymbol{\nabla}\varphi\boldsymbol{\nabla}\psi$ term in Eq. (5)]. The additional constraint that $\gamma_{AB} = \gamma_{AC} = \gamma_{BC}$ gives the ratio between the coefficients in the gradient terms to be $\kappa_\varphi = \kappa_\psi/3$. The constraint that the mobilities of all the phases be equal yields $M_\varphi = 3M_\psi$ [17]. We note that these constraints on the values of the interfacial tensions and mobilities are not necessary conditions to observe the behavior described below. In fact, as we discuss in the next section, a range of different interfacial tensions and mobilities will yield results similar to those presented herein.

To update the values in Eqs. (2) and (3), we used the cell dynamical system method [26]. Details on how this method was implemented for a reactive system with two order parameters are given in the Appendix. The Appendix also gives the values of parameters used in these simulations.

We emphasize that when the C component is absent ($\psi=0$), the above model reduces to a well-known model for block copolymers [27,28] or reactive polymer blends [9,11]. In this case, the evolution of the reactive AB system is governed solely by Eq. (2) and the morphology of the mixture resembles the lamellar structure formed by microphase-separated symmetric diblock copolymers [9,29]. (In the context of our work, we only consider reactive blends, and do not consider diblock copolymers.) For such reactive binary mixtures, a linear stability analysis gives the growth rate, $w_\varphi(k)$, for the kth mode of the fluctuations of the order parameter around the homogeneous value $\varphi=0$ as

$$w_\varphi(k) = 2M_\varphi[a_{20}k^2 - \kappa_\varphi k^4] - 2\Gamma. \tag{7}$$

The roots of this characteristic equation give two critical wave numbers, $k^2_{crit,\pm}=\frac{a_{20}}{2\kappa_\varphi}\left[1\pm\sqrt{1-\frac{4\Gamma\kappa_\varphi}{M_\varphi a_{20}^2}}\right]$, if the reaction rate coefficient is sufficiently small that $\Gamma < a_{20}^2 M_\varphi/4\kappa_\varphi$. The existence of a lower critical wave number due to the reaction term means that fluctuations with the small wave numbers $k < k_{crit,-}$ are suppressed. In other words, only fluctuations with wavelengths in the range $\frac{2\pi}{k_{crit,+}} < \lambda < \frac{2\pi}{k_{crit,-}}$ can grow in such systems. Thus, reactions such as those in Eq. (1) arrest domain growth in binary mixtures at a characteristic wavelength λ, which is defined by the parameters Γ, M_φ, and κ_φ and can be found by minimizing the total free energy in the system (which includes the reactive term). We also note that for large reaction rate coefficients $\Gamma > a_{20}^2/4\kappa_\varphi M_\varphi$, any fluctuations of the order parameter are suppressed, so that the mixture will remain homogeneously mixed.

It has been shown [11,27] that Eq. (2) can be rewritten as

$$\frac{\partial\varphi}{\partial t} = M_\varphi \nabla^2 \frac{\delta\tilde{F}(\varphi,\psi)}{\delta\varphi}, \tag{8}$$

where

$$\tilde{F}(\varphi,\psi) = F(\varphi,\psi) + \frac{\Gamma}{M_\varphi V}\int d\mathbf{r}d\mathbf{r}'\, G(\mathbf{r}-\mathbf{r}')\varphi(\mathbf{r})\varphi(\mathbf{r}') \tag{9}$$

and the Green's function $G(\mathbf{r}-\mathbf{r}')$ can be found from Poisson's equation $\nabla^2 G(\mathbf{r}-\mathbf{r}')=-\delta(\mathbf{r}-\mathbf{r}')$ with the appropriate boundary conditions [11,27]. Below, we will use Eq. (9) to estimate the total free energy of the ternary system.

Finally, we note that a linear stability analysis of both Eqs. (2) and (3) for the ternary case gives a growth rate $w_\psi(k)$ for the kth mode of the fluctuations of the second-order parameter around the homogeneous value $\psi=0$ as

$$w_\psi(k) = 2M_\psi[a_{02}k^2 - \kappa_\psi k^4], \tag{10}$$

while the growth rate $w_\varphi(k)$ for the kth mode of the fluctuations of the first-order parameter is still given by Eq. (7). In other words, there is no lower critical wave number for the second-order parameter fluctuations and all large wavelength fluctuations will grow. This means that in our ternary system, a suppression of the large wavelength fluctuations (i.e., a freezing of the evolution of the domains at some characteristic wavelength) is only expected to occur within the A/B domains and the growth of the C domains is not suppressed. [We note that this behavior was in fact observed in earlier simulations [in two dimensions (2D)] on copolymer/homopolymer blends [24].]

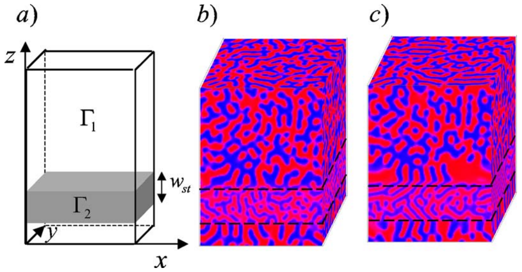

FIG. 1. (Color online) (a) Schematic of the system. Unless specified otherwise, for the calculations presented herein, the simulation box is 120×120×150 lattice sites in size and the width of the Γ_2 region is $w_{st}=40$ lattice sites (the positions of the lower and upper boundaries of the Γ_2 region are at $z=20$ and at $z=60$, respectively). (b), (c) Evolution of the binary AB blend in the simulation box shown schematically in (a). Here, $\Gamma_1=0.003$ and $\Gamma_2=0.01$, and the simulation times are (b) $t=10^4$ and (c) $t=7\times10^4$. The A component is shown in light gray (blue online) and B component is shown in dark gray (red online).

In the Results and Discussion section, we first consider the evolution of ternary systems where the irradiation is spatially nonuniform, but constant in time. In other words, we study the structural evolution within a simulation box that consists of two regions and each of these regions is assumed to have a different reaction rate coefficient. Then, we consider the evolution of both binary and ternary systems in the cases where we also vary the reactions rate coefficients in time. In the last section of the paper, we show how one can create defect-free materials using the proposed technique. We also briefly discuss the effects of the attenuation of the light intensity within the thickness of the sample and we relate our simulation parameters to actual physical values.

III. RESULTS AND DISCUSSION

A. Spatially nonuniform, constant-light irradiation

Using the approach outlined above, we consider the evolution of binary and ternary blends within a three-dimensional simulation box, which is shown schematically in Fig. 1(a). Periodic boundary conditions are applied in the x, y, and z directions. We assume that the entire box is irradiated with a uniform background light. We will refer to the reaction rate coefficient corresponding to the background light as Γ_1. In all the simulations described herein, we fix $\Gamma_1=0.003$. To this uniformly irradiated system, we introduce a spatially localized, secondary light source, which is represented by the dark stripe in Fig. 1(a). We focus on the case where the intensity of the secondary light is higher than that of the background light. The higher-intensity, secondary light source locally increases the reaction rate coefficients to $\Gamma_2 > \Gamma_1$. (Within this region of higher light intensity, we again assume that the rate coefficients for the forward and reverse reactions are the same—i.e., $\Gamma_2^+ = \Gamma_2^- \equiv \Gamma_2$.) For the studies described in this section, we assume that these reaction rates do not change in time.

To facilitate our understanding of the behavior of ternary reactive mixtures under such spatially nonuniform irradiation, we first consider the response of a binary reactive blend to the same conditions. The initial condition for these simulations is a homogeneous *AB* mixture with a random fluctuation of the order parameter around its average value, $\langle\varphi\rangle = 0$. [We chose the standard deviation to be equal to 0.03; however, any reasonably small value ($<< 1$) can be chosen.] Here, $\Gamma_1 = 0.003$ and $\Gamma_2 = 0.01$. Figures 1(b) and 1(c) show the morphology of the binary mixture at early times and at late times, respectively. As expected, the domains resemble the lamellar morphology of microphase-separated, symmetric diblock copolymers [9,11,27,28]. Figures 1(b) and 1(c) clearly illustrates that the thickness of the lamellae are smaller and the intermixing is higher (i.e., the bulk value of the order parameter is lower) within the Γ_2 region.

The above results agree with earlier studies on *AB* binary reactive mixtures [9,11]. Moreover, it has been shown [11] that for the binary case, it is possible to use a single-mode approximation (in 1D) for the order parameter $\varphi = \varphi_0 \cos kx$ to successfully estimate the bulk value of the order parameter φ_0 and the equilibrium value of the wave number k for a given value of Γ. (Note that this approximation is valid for small φ or relatively high Γ.) Choosing the Green's function in Eq. (9) to be of the form $G(x-x') = -\frac{|x-x'|}{2}$ [11,27] and minimizing the total free energy with respect to k and φ_0 [11], we obtain $k = \sqrt[4]{\frac{\Gamma}{M_\varphi \kappa_\varphi}}$ and $\varphi_0 = \sqrt{\frac{2a_{20}}{3a_{40}}}\sqrt{1 - \frac{2}{a_{20}}\sqrt{\frac{\kappa_\varphi \Gamma}{M_\varphi}}}$. The latter expression clearly indicates that φ_0 decreases with increases in Γ. In addition, using the above expressions for k and φ_0, we rewrite the total free energy density, Eq. (9), for this 1D single-mode approximation as

$$F_{AB}(\Gamma) = -\frac{1}{6a_{40}M_\varphi}\left[-2\sqrt{\kappa_\varphi \Gamma} + a_{20}\sqrt{M_\varphi}\right]^2. \tag{11}$$

The dependence of the bulk value of the order parameter φ_0 on the values of Γ is shown in Fig. 2; the circles mark the simulations, and the solid line is the analytical expression for φ_0 given above. The good agreement between the simulation results and analytical expression for φ_0 indicates that the above approximation is valid for the wide range of Γ in our 3D simulations. This result also suggests that the formula in Eq. (11) can be used to estimate the free energy of such binary reactive systems (see inset in Fig. 2).

In the next series of simulations, we turn our attention to studies of the evolution of the ternary blends under the spatially nonuniform, constant light irradiation. Figure 3 shows the time evolution of the ternary system within the same simulation box as in Fig. 1(a). In this case, the initial condition is a homogeneous *ABC* mixture with a random fluctuation of both order parameters around their average values, $\langle\varphi\rangle = 0$, and $\langle\psi\rangle = 0.27$, respectively. (Here again, the standard deviation about the average value is taken to be to 0.03.) Strictly speaking, in order to fully describe the system, one has to plot the distribution of the both order parameters φ and ψ. However, since the *C* component phase separates from the *AB* mixture (i.e., within the *C* domains $\psi \approx 1$ and $\varphi \approx 0$), we can easily show the evolution of the system by plotting the value of the first-order parameter φ for all the points in space for which the condition $\psi < \tilde{\psi} = 0.65$ is satisfied and by plotting the distribution of ψ for all the points in space for which $\psi \geqslant \tilde{\psi}$. In other words, where the *C* component is present and the *AB* component is predominantly absent within the simulation box, we plot the only *C* component, and where the *C* component is predominantly absent, we plot the only *AB* order parameter. We also note that such graphical representation leads to the interface between *C* and *AB* looking somewhat sharper then it is in the data.

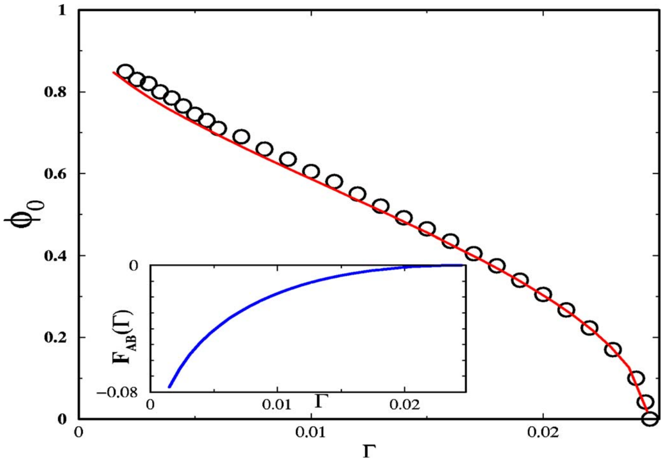

FIG. 2. (Color online) Dependence of the bulk values of the order parameter φ_0 on the reaction rate coefficient Γ. The circles show simulation data, and the line is $\varphi_0 = \sqrt{\frac{2a_{20}}{3a_{40}}}\sqrt{1 - \frac{2}{a_{20}}\sqrt{\frac{\kappa_\varphi \Gamma}{M_\varphi}}}$ with $\kappa_\varphi = 0.25$, $M_\varphi = 0.076$, $a_{20} = 0.569$, and $a_{40} = 0.398$ (see the Appendix). The inset shows the dependence of free energy on the reaction rate coefficient Γ as given by Eq. (11) with the above simulation parameters.

The snapshots of the structural development of the mixture illustrate a number of processes that are occurring simultaneously: (i) phase separation among all three components, (ii) the competition between the reaction and phase separa-

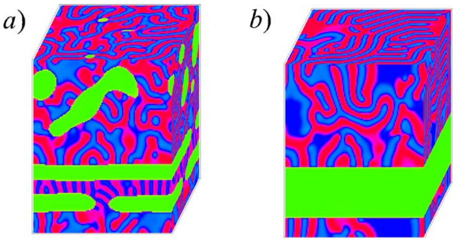

FIG. 3. (Color online) Evolution of the ternary system within the simulation box shown in Fig. 1. Here, $\Gamma_1 = 0.003$, $\Gamma_2 = 0.01$. The images show morphologies of the ternary mixture for the simulation times $t = 5 \times 10^4$ and $t = 5 \times 10^5$ for (a) and (b), respectively. Here and in all the morphologies of ternary mixtures below, the *C* component is shown in lightest gray (green online); *A* and *B* components are shown in two darker shades of gray (blue and red online) and the interfaces between *A* and *B* components are shown in black (pink online).

tion that defines the characteristic mixing and length scale within the *AB* domains (for both the Γ_1 and Γ_2 regions), and (iii) migration of the *C* component to the Γ_2 region (the region with the higher reaction rate coefficient). At late times, we observe saturation of the Γ_2 region with the *C* component [see Fig. 3(b)]. We also observe that the *AB* domains are orientated perpendicular to the boundaries of the *C* stripe. We emphasize that the amount of *C* was chosen such that *C* fills the Γ_2 region. If there is too much of the *C* component in the system, the final *C* domain still forms around the Γ_2 stripe, but the positions of the interfaces between the *C* and *AB* domains are influenced by the concentration of *C*. If there is too little of the *C* component in the system, it will not completely fill the whole Γ_2 stripe, so that a droplet of *C* is formed within the Γ_2 stripe.

The reason the *C* component migrates to the higher-intensity region (as shown in Fig. 3) is that in this manner, the total free energy of the system is minimized. In order to understand the latter effect, we recall that the total free energy of an *AB binary* reactive mixture, $\tilde{F}(\varphi,0)$ [as defined in Eq. (9)], monotonically increases with increasing Γ [see Eq. (11) and inset in Fig. 2]. Therefore, the total free energy density of the *binary AB* mixture is higher in the Γ_2 region than in the Γ_1 region. In the *ternary* case, the *A* and *B* components diffuse to the lower-free-energy region (i.e., to the Γ_1 region or in the other words, away from the Γ_2 region); thus, the Γ_2 region becomes more and more "depleted" of *AB* domains and "enriched" with the nonreactive *C* component. Therefore, in a system that consists of two regions, one with a higher and one with a lower reaction rate coefficient, the *A* and *B* components diffuse out of the region with the higher reaction rate coefficient, while the *C component migrates into this region*. At late times, the *C* component will be always located in the region with the higher reaction rate coefficient, since in this way, the total free energy within the system [see Eq. (9)] is minimized.

In order to quantitatively characterize the migration of the *C* component to the Γ_2 regions, we plot the actual volume fraction of *C* within this region, C_0, as a function of time for different values of Γ_2. Specifically, we calculate

$$C_0 = \frac{1}{V_{\Gamma_2}} \oint_{\Gamma_2} \psi(\mathbf{r},t)\, d\mathbf{r}. \tag{12}$$

Figure 4(a) shows that at late times, *C* always diffuses to the Γ_2 region; however, the rate at which this region becomes saturated strongly depends on the values of Γ_2. In particular, the domain saturates faster for higher values of Γ_2. The gain in the total free energy for "replacing" the *AB* domains with the *C* domains within the Γ_2 region increases with increases in the value of Γ_2/Γ_1; the greater gain in free energy provides a driving force for the more rapid migration of the *C* component.

Figure 4(b) further illustrates the functional dependence of the characteristic time that is needed for the *C* component to migrate to the Γ_2 regions. The curves marked with the circles and squares give the respective characteristic times $\tau_{0.8}$ and $\tau_{0.96}$ needed to reach the saturation values of $C_0=0.8$ and $C_0=0.96$ for the system shown in Fig. 3 for the chosen values of Γ_2 (the symbols represent the simulation data). All the above results are obtained for a fixed value of interfacial tension, fixed concentration of *C* ($\langle\psi\rangle=0.27$) and fixed geometry [as in Fig. 1(a)]. The dashed lines in Fig. 4(b) are the fitting curves, which we have chosen to be of the functional form $A/[F_{AB}(\Gamma_2)-F_{AB}(\Gamma_1)]$, where *A* is a fitting constant and $F_{AB}(\Gamma)$ is given by Eq. (11). As one might expect from the above discussion, the characteristic time is indeed found to be inversely proportional to the differences in the free energy between the Γ_2 and Γ_1 regions.

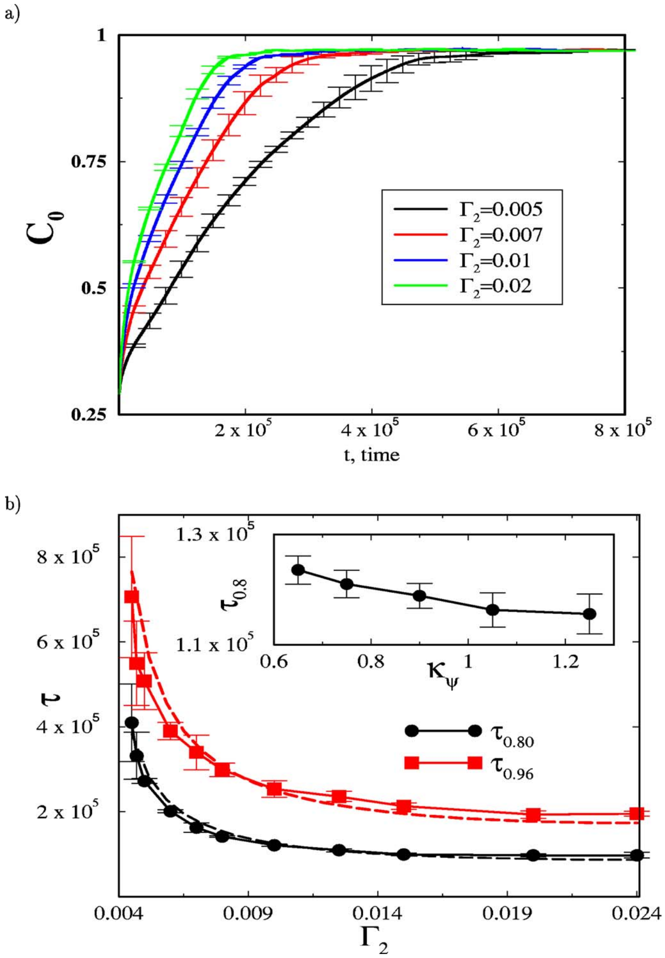

FIG. 4. (Color online) (a) Time evolution of the volume fraction of the *C* component within the Γ_2 stripe for the system shown schematically in Fig. 1(a). (b) Characteristic times $\tau_{0.8}$ and $\tau_{0.96}$ needed to reach the volume fraction of $C_0=0.8$ and $C_0=0.96$ for the chosen values of Γ_2 (the circles and squares represent the respective simulation data). The dashed lines in (b) are the fitting curves, $A/[F_{AB}(\Gamma_2)-F_{AB}(\Gamma_1)]$, where the fitting constant *A* is 5×10^3 and 10^4 for $\tau_{0.8}$ and $\tau_{0.96}$, respectively. The inset in (b) shows the characteristic times $\tau_{0.8}$ needed to reach the volume fraction of $C_0=0.8$ for the chosen values of κ_ψ at fixed $\Gamma_2=0.01$ (the circles represent the respective simulation data).

Additional simulation studies show that the characteristic saturation time τ_{C_0} decreases when we use higher concentrations of *C* (and correspondingly decrease L_Z so that that the total amount of *C* in the system is the exact amount that is needed to cover the Γ_2 region) or when we increase the interfacial tension γ_{AC}. In the latter case, however, the decrease

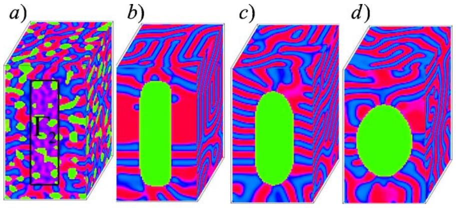

FIG. 5. (Color online) Saturation of the Γ_2 region, which occupies a rectangular parallelepiped of size $22\times 60\times 94$ lattice sites and is located within a simulation box of size $60\times 60\times 120$ lattice sites. (a) $\Gamma_2=0.02$, $\kappa_\psi=0.75$, $t=10^3$; (b) $\Gamma_2=0.02$, $\kappa_\psi=0.75$, $t=10^6$; (c) $\Gamma_2=0.005$, $\kappa_\psi=0.75$, $t=10^6$; (d) $\Gamma_2=0.005$, $\kappa_\psi=1.25$, $t=10^6$.

in τ_{C_0} is relatively small; for example, increasing κ_ψ from $\kappa_\psi=0.6$ to $\kappa_\psi=1.25$ (which corresponds to 39% increase in γ_{AC}) leads to $\approx 6\%$ decrease in $\tau_{0.8}$ [see inset in Fig. 4(b)]. We emphasize that at late times in each of the above cases, the C component fills the Γ_2 region.

It is particularly noteworthy that the effect of the migration of C to the higher-intensity regions is independent of the properties of the local free energy of the C component. For example, we varied the depth of the minima of free energy that corresponds to the pure C component [i.e., we altered the appropriate coefficients in Eq. (5)]. We found that the migration of C to the Γ_2 regions is observed for any chosen parameters. These observations support the above theoretical arguments; i.e., the migration of C to the higher Γ region happens because the AB blend is diffusing away from this region, and C simply occupies available space. In other words, the effect depends mostly on the AB properties and essentially does not depend on the properties of the C component (for the range of parameters explored in this study).

In the next series of simulations, we examine the migration of C in the case where the Γ_2 region is a rectangular parallelepiped, which is located in the center of the xz plane, and spans the simulation box in the y direction [as indicated by the black rectangle in Fig. 5(a)]. Figures 5(a) and 5(b) show the early- and late-time morphologies for the case where $\Gamma_2=0.02$ and $\kappa_\psi=0.75$, respectively. One can clearly see that the C component is located within the Γ_2 region at late times; i.e., the writing is relatively successful, with the imperfections in the corners of the parallelepiped being comparable in size to the interfacial width. At the lower value of $\Gamma_2=0.005$, Fig. 5(c) indicates that the writing is less successful. Although the C component still migrates to the Γ_2 region, the imperfections become much more distinct. Finally, Fig. 5(d) shows the late-time morphology for the case of the least successful writing, where the C domain forms a cylinder instead of the rectangular parallelepiped. In the latter case, in addition to a decreased value of $\Gamma_2=0.005$, we chose a relatively high value of the interfacial tension between the A (B) and C components, $\kappa_\psi=1.25$.

To predict which situation will occur for a given set of parameters [i.e., as in Fig. 5(b) and 5(c), or 5(d)], one has to consider the relative magnitudes of the two distinct contributions to the total free energy. In the case shown in Fig. 5(b), the free energy within the cube is minimized because the A and B components are essentially absent from the Γ_2 region (except for a relatively small amount within the corners of the Γ_2 region; we assume this amount to be negligibly small in the following estimates). However, there is some increase in the total free energy due to the relatively large interfacial area between the A (B) and C domains. The total free energy of the configuration shown in Fig. 5(b) can be estimated as

$$\Psi_{tot}^{sharp} \approx F_{AB}(\Gamma_1)(V - V_{\Gamma_2}) + A_{\Gamma_2}\gamma_{AC} + F_C V_{\Gamma_2}, \tag{13}$$

where $F_{AB}(\Gamma_1)$ is the free energy density of the A and B domains with the Γ_1 region and V and V_{Γ_2} are the volumes of the simulation box and the Γ_2 region, respectively. The parameter A_{Γ_2} is the surface area of the Γ_2 region and F_C is the free energy density within the C domain. Note that the volume V_C and the surface area A_C of the C domain in the above case are taken to be equal to the respective volume V_{Γ_2} and to the surface area A_{Γ_2} of the Γ_2 region.

In contrast, in the case of Fig. 5(d), the interfacial area between the A (B) and C domains is at a minimum value; however, there is some loss in the total free energy due to the presence of A and B domains within the Γ_2 region. The total free energy of the configuration shown in Fig. 5(d) can be estimated as

$$\Psi_{tot}^{cyl} \approx F_{AB}(\Gamma_1)(V - V_{\Gamma_2} - \Delta V) + F_{AB}(\Gamma_2)\Delta V + A_C\gamma_{AC} + F_C V_C, \tag{14}$$

where ΔV is the volume of the Γ_2 region occupied by A and B domains. Note that in this case the volumes and the surface areas of the C domain and of the respective values for the Γ_2 region are distinctly different.

A sharper domain of C [as in Fig. 5(b)] will be formed if the decrease in the total free energy due to the A and B domains migrating out of the Γ_2 region exceeds the increase of the free energy due to the formation of a relatively large interface—i.e., if $\Psi_{tot}^{sharp} < \Psi_{tot}^{cyl}$, which, using the above estimates, can be rewritten as

$$\Delta V[F_{AB}(\Gamma_2) - F_{AB}(\Gamma_1)] > (A_{\Gamma_2} - A_C)\gamma_{AC}. \tag{15}$$

The above condition basically states that a sharper C domain can be written with higher Γ_2 and lower γ_{AC} values. For our simulation values and for the geometry in Fig. 5, the condition in Eq. (15) is only satisfied for the case shown in Fig. 5(b) (specifically, in this case we have $\Delta V[F_{AB}(\Gamma_2) - F_{AB}(\Gamma_1)] \approx 2.3(A_{\Gamma_2} - A_C)\gamma_{AC}$).

We also note that for the parameters used for the case shown in Fig. 5(c), even though the condition in Eq. (15) is not satisfied, the actual values on the left and right sides of the inequality are relatively close ($\Delta V[F_{AB}(\Gamma_2) - F_{AB}(\Gamma_1)] \approx 0.7(A_{\Gamma_2} - A_C)\gamma_{AC}$). The latter values indicate that there is a strong competition between the two mechanisms that contribute to the decrease of the total free energy (i.e., the migration of the A and B domains from the Γ_2 regions and the decrease of the interfacial area of the C domain); this competition yields the final shape of the C domain.

And finally, for the case shown in Fig. 5(d), we have $\Delta V[F_{AB}(\Gamma_2) - F_{AB}(\Gamma_1)] \approx 0.4(A_{\Gamma_2} - A_C)\gamma_{AC}$. In this case, the cylindrical configuration clearly corresponds to the minimum of the total free energy. We note that even though we have written Eq. (15) for the specific case where the Γ_2 region has

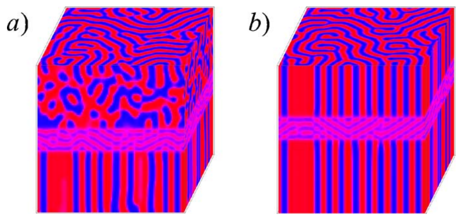

FIG. 6. (Color online) Evolution of the binary system, combed with a rastering speed of $\nu=0.001$. Here, $\Gamma_2=0.02$, and the corresponding simulation time steps are (a) $t=5\times10^4$ and (b) $t=3\times10^5$. Here and in all the following simulations, we set the width of the moving Γ_2 region to $w_{mov}=20$ lattice sites.

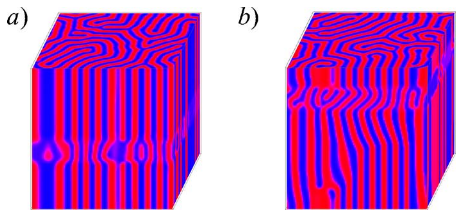

FIG. 7. (Color online) Late-time morphology for unsuccessful combing with $\Gamma_2=0.007$. The rastering velocities and the corresponding times are (a) $\nu=0.002$, $t=8\times10^5$; (b) $\nu=0.0005$, $t=6\times10^5$.

the form of a rectangular parallelepiped and showed that the above condition describes our simulation results, the arguments we used to derive Eq. (15) are quite general and the same condition can be used to estimate the sharpness of the written pattern for basically any chosen shape of the Γ_2 region.

B. Spatially nonuniform, dynamically controlled light irradiation

1. Ordering within the binary systems

In this section, we examine the ordering in binary systems as we move the secondary, higher intensity light [the dark Γ_2 region in Fig. 1(a)] from the bottom to the top of the entire sample. As shown in our previous study [3,4], by rastering this light over a 2D sample (i.e., a thin polymeric film), we could effectively "comb out" the defects within the system, provided that the Γ_2/Γ_1 ratio is sufficiently high and the "combing" speed is lower than a specified critical value. In the current work, we study the ordering in 3D, where a slab with a reaction rate coefficient of Γ_2 is moved with a velocity ν.

Figure 6 shows the time evolution in an *AB* system that is being ordered or "combed" with the moving light (the Γ_2 region). Here, $\Gamma_2=0.02$ and the thickness of this region is $w_{mov}=20$ lattice sites. This slab is being moved with a velocity of $v=0.001$ lattice sites per simulation time step. As the Γ_2 region passes through the sample, the underlying domains reorient perpendicular to the moving slab (i.e., along the "combing" direction). Recall that the domains are smaller and more intermixed within the Γ_2 region [see Figs. 1(b), 1(c), and 2]. Consequently, these domains are relatively neutral with respect to the Γ_1 domains. In the presence of a neutral boundary, the neighboring *A* and *B* domains within the Γ_1 region will form a 90° contact angle with this interface [30]. Another way to understand the effect that this neutral layer has on the neighboring Γ_1 regions is to draw an analogy between this system and the behavior of diblock copolymers in the presence of neutral or nonselective walls. Recall that the lamellar domains of symmetric diblocks align perpendicular to neutral walls since this configuration lowers the free energy of the system [31]. As the Γ_2 stripe is moved from the bottom to the top of the sample, the underlying Γ_1 domains become more oriented along z and, in this manner, the defects along this direction are effectively "combed out" of the material.

Similar to the 2D case [4], the efficiency of the combing process depends on the velocity of the moving stripe and on the value of Γ_2 relative to Γ_1. For example, in the case shown in Fig. 6, Γ_2 is sufficiently high that the *A* and *B* phases are almost intermixed within the stripe; consequently, the combing is highly efficient. For lower values of Γ_2 within the stripe (where we still maintain the constraint that $\Gamma_2>\Gamma_1$), the efficiency of the combing strongly depends on the combing velocity. Figure 7 illustrates this point for both higher [see Fig. 7(a)] and lower [see Fig 7(b)] rastering velocities for a fixed value of $\Gamma_2=0.007$. We note that these values of the rastering speeds, as well as all the values used later in this work, are lower than the critical velocity $\nu_{\max}\approx2\Gamma_2 w_{mov}$ [3,4]. If v is on the order of or greater than $v_{\max}$, then the secondary light is being rastered too quickly for the lamellar domains within the Γ_2 stripe to reach both their equilibrium size and bulk order parameter (i.e., for the domains to become intermixed). Given this constraint, it can be seen that the ordering is significantly better for the higher rastering velocity. At the lower rastering velocity [Fig. 7(b)], the stripe is moving sufficiently slowly that the Γ_2 domains are reorienting in order to coincide with the domains in the neighboring Γ_1 region. Due to the difference in sizes, a perfect match between the different domains is not possible and, therefore, the motion of the stripe leads to the formation of the distorted domains.

To quantitatively characterize the ordering along the z direction, we use the following measure:

$$\beta_Z(t)=\langle\langle\varphi(t)\rangle_Z^2/\langle\varphi(t)^2\rangle_Z\rangle_{X,Y}. \qquad (16)$$

The system is completely ordered along z when $\beta_Z=1$. The above definition for β_Z is the 3D analog of the definition we implemented in the 2D case [3,4]. We emphasize that this measure only allows us to calculate the ordering in the z direction and does not account for any order or disorder in the x,y directions. In other words, the ordering along z is complete if all the *AB* interfaces are oriented along the z direction, independent of the thickness and orientation of these domains in the x and y directions. Note that in Eq. (16), the average values $(\langle\cdots\rangle_Z,\langle\cdots\rangle_{X,Y})$ are calculated everywhere within the box except within the moving Γ_2 region.

In Fig. 8, we plot the evolution of β_z within the system as regions with either $\Gamma_2=0.007$, $\Gamma_2=0.01$, or $\Gamma_2=0.02$ are rastered through the sample. For each value of Γ_2, we calculate the ordering for three different rastering velocities; each data point (with error bars) represents an average over three inde-

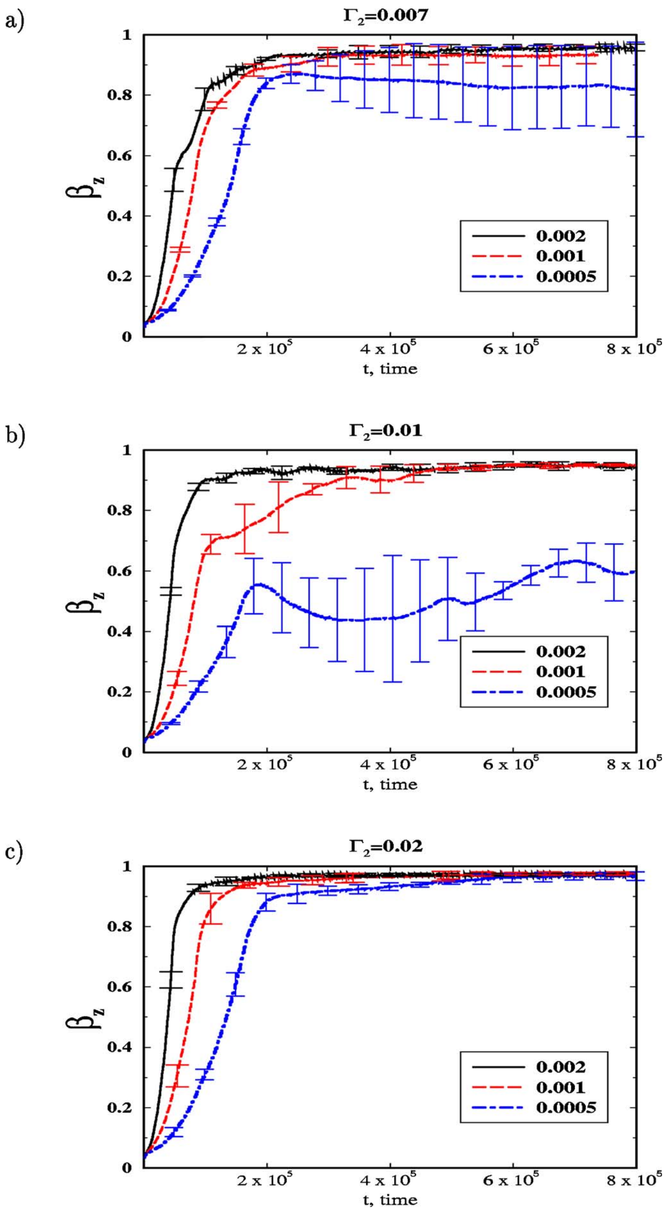

FIG. 8. (Color online) Evolution of the ordering, β_z, for (a) Γ_2=0.007, (b) Γ_2=0.01, and (c) Γ_2=0.02. For all the cases, solid, dashed, and dot-dashed curves represent an average over three independent runs with the values of rastering velocities taken to be ν=0.002, ν=0.001, and ν=0.001, respectively (see corresponding legends).

pendent runs. A common feature of all the plots in Fig. 8 is the fast growth of the ordering within the sample during the first passage of the Γ_2 region over the sample. In each curve, the saturation of the ordering (i.e., when β_z reaches its equilibrium value for the given rastering speed and the value of Γ_2) happens at the beginning of the second passage of the Γ_2 region over the sample. In fact, we observed that a single passage is enough to obtain a value of β_z that is close to its equilibrium value everywhere within the sample, except at the bottom portion of the simulation box, where the ordering is slightly distorted due to the periodic boundary conditions. The latter observation explains the improved ordering during the beginning of the second passage.

Another common feature of all the examples in Fig. 8 is the high degree of ordering that is obtained at relatively high velocities [see solid lines in Figs. 8(a)–8(c)]. The ordering at the lowest rastering velocity is the poorest for both intermediate values of Γ_2 (i.e., for Γ_2=0.007 and Γ_2=0.01). As was shown in the example in Fig. 7, when the Γ_2 region is moved sufficiently slowly and Γ_2 is relatively small (as compared to Γ_1), the domains within this stripe undergo a rearrangement to "match up" with the domains in the neighboring Γ_1 region; this behavior effectively reduces the ordering in z since this matching is not possible for domains with different sizes. In addition, the increase in the ordering of the domains in the z direction can be slightly reduced due to the fact that the domains are observed to reorient in the the x,y directions.

The situation is different for the slow movement of the slab with a relatively high value of Γ_2 [see the dash-dotted line in Fig. 8(c)]. In the latter case, the intermixing is sufficiently high that the Γ_2 region is relatively neutral with respect to the Γ_1 region; hence, the perpendicular orientation of the domains in the Γ_1 region is realized at each moment in time and is propagated along the sample.

We also note here that the error bars in Fig. 8 are small for the cases of successful combing, indicating that the combing is robust and does not depend on the initial conditions. On the other hand, the error bars are relatively large for the cases of nonsuccessful combing; this indicates that if a structure with defects is formed, the actual morphology and, therefore, the degree of ordering, depends to some extent on the initial conditions.

Summarizing this section, we found that the rastering of the Γ_2 region throughout the sample in a selected direction can be used to introduce an ordering in this direction (the z direction in the above example). However, rastering along one direction cannot be used to introduce order in all directions. In order to achieve ordering in all directions, a similar technique can be applied a second time in the x direction. In additional simulation studies, we selected a sample that is ordered in the z direction [as in Fig. 6(b)], removed the Γ_2 region that was used during the first stage of the process, and instead, introduced another Γ_2 region, which was rastered along the x direction, from the left to the right. The late-time morphology in these cases exhibited a high degree of order in all directions since the rastering along x aligns the AB interfaces along this direction (due to the moving "neutral" boundary effect discussed above). In the other words, as the Γ_2 stripe moves from the left to right, it effectively "transfers" the ordering along z on its left side throughout the sample. Below, we illustrate how to apply such a two-step process to introduce ordering within the ternary systems.

2. Ordering within the ternary systems

In this section, we consider a ternary system similar to one described in Sec. III A, except that we now introduce a moving slab, characterized by the higher reaction rates coefficients, to introduce ordering within the AB domains. In particular, we consider the system shown schematically in Fig. 9(a). The images in Figs. 9(c) and 9(d) llustrate the structural evolution in this system. The two major effects that we de-

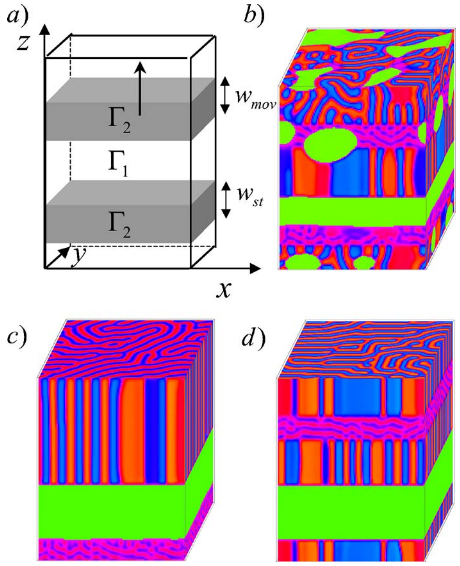

FIG. 9. (Color online) (a) Schematic of the system with two Γ_2 regions. The width of the stationary Γ_2 region (lower dark region) is $w_{st}=40$ lattice sites with the positions of the lower and upper boundaries at $z=20$ and at $z=60$, respectively (same as in the schematic in Fig. 1). The width of the moving Γ_2 region (upper dark region) is 20 lattice sites. (b)–(d) Evolution of the ordering in the ternary system, rastered with a high-intensity region with $\Gamma_2=0.02$ along the z direction with a rastering velocity of $\nu=0.001$. The corresponding times are (b) $t=10^5$, (c) $t=6\times10^5$, and (d) $t=10^6$.

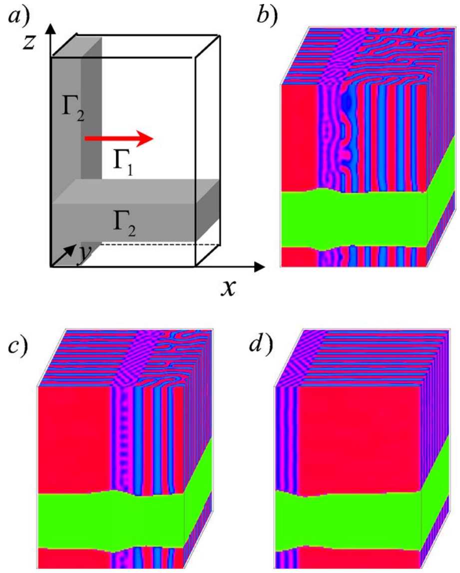

FIG. 10. (Color online) (a) Schematic of the second step of the two step combing process: the horizontal Γ_2 region remains the same as in the schematic shown in (a), but the moving Γ_2 region ($w_{mov}=20$) is oriented vertically and moves along the x direction (from the left to the right). (b)–(d) Snapshots of the ternary morphology at the following simulation time steps: (b) $t=3\times10^4$, (c) $t=6\times10^4$, and (d) $t=6\times10^5$.

scribed above are occurring simultaneously in this system: (i) the C component migrates to the stationary Γ_2 region and (ii) the moving Γ_2 region combs out the defects within the AB domains along the combing direction.

To achieve ordering within all three directions, we introduce a second step, as shown schematically in Fig. 10(a). Here, we take the morphology that was ordered along the z direction during the first step (as in Fig. 9), remove the mobile Γ_2 region that was utilized in this first step, and instead, introduce another Γ_2 region, which we now raster along the x direction, from the left to the right [see Fig. 10(a)]. We keep the stationary Γ_2 region in the same position as in the first step [see Fig. 9(a)]. An example of the structural evolution in this system is shown in Figs. 10(b)–10(d). As the initial state for this simulation, we took the late-time morphology from the example shown in Fig. 9 (at time $t=6.25\times10^5$). The images in Figs. 10(b)–10(d) llustrate that rastering along the x direction aligns the A/B interfaces along x; this behavior is attributable to the "neutral" moving boundary, as described above. The late time morphology [see Fig. 10(d)] exhibits a high degree of order in all three directions.

It is worth noting the distortion of the C region at the places where the moving Γ_2 region crosses the stationary Γ_2 region and the fact that these distortions relax away from the moving Γ_2 region. These distortions appear for the following reason: at each moment of time, some portion of the C component from the stationary Γ_2 region diffuses to the moving Γ_2 region because the minimization of the total free energy is the same when the C component occupies either of these Γ_2 regions. As the mobile Γ_2 region is swept across the remainder of the sample, the C component returns back to its position within the stationary Γ_2 region (see Fig. 10). Therefore, one can expect that the above distortions are smaller for a more rapidly moving Γ_2 region and for a lower mobility M_ψ of the C component. If the mobility of C is slow or if the Γ_2 region is moved sufficiently quickly, the C component does not have enough time to "respond" to the moving Γ_2 region and this is in fact what we observe in additional simulation studies.

The images in Fig. 10 illustrate the fact that two steps are needed to create the final, ordered 3D structure [as in Fig. 10(d)]. We note that the critical role of the first step (combing along z) in the formation of the final structure lies in ordering only within the left side of the image in Fig. 10(b). In other words, as the Γ_2 stripe moves from the left to right, it effectively "transfers" the ordering along z on its left side throughout the sample. Therefore, to create the morphology shown in Fig. 10(d) in an efficient manner, one does not necessarily have to carry out the vertical "combing" for the entire sample; it is sufficient to "comb" along z for only a small longitudinal section of the sample. (This will be discussed in detail in future work.)

In order to quantify the degree of order within a sample such as that in Fig. 10(d), we calculate the ordering in the x direction in the same way that we calculated the ordering in the z direction,

$$\beta_X(t) = \langle\langle\varphi(t)\rangle_X^2/\langle\varphi(t)^2\rangle_X\rangle_{Y,Z}. \tag{17}$$

In Fig. 11, we plot the evolution of β_X within the system as a region with $\Gamma_2=0.02$ is rastered from the left to the right [as in Fig. 10(a)] through the sample at three different rastering velocities; each curve is an average of three indepen-

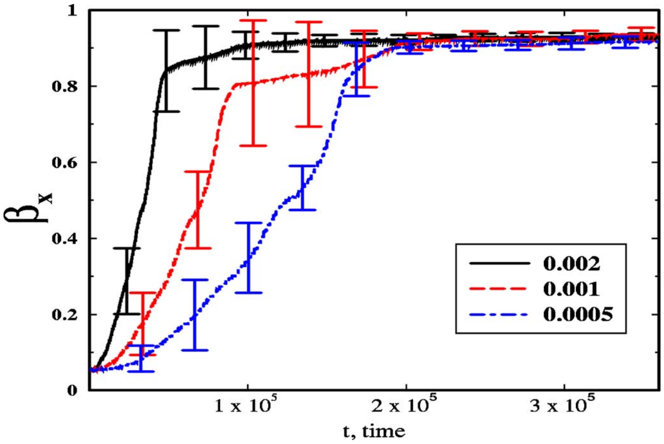

FIG. 11. (Color online) Evolution of the ordering, β_x, in the ternary system shown schematically in Fig. 10. Solid, dashed, and dot-dashed curves represent an average over the three independent runs with the values of rastering velocities $\nu=0.002$, $\nu=0.001$, and $\nu=0.005$, respectively (see legend). Here, we use $\Gamma_2=0.02$.

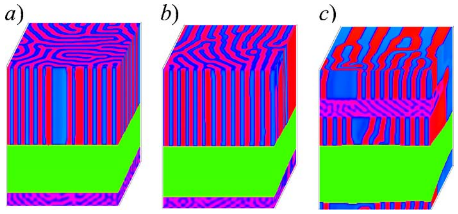

FIG. 12. (Color online) Late-time morphologies in the ternary system (its schematic is shown in Fig. 10), for the following values of the characteristic length scales (in lattice sites) of light attenuation, R_0: (a) $R_0=360$, (b) $R_0=120$, (c) $R_0=60$, and (d) $R_0=30$. The corresponding simulation time steps are (a)–(c) $t=6\times10^5$ and (d) $t=8\times10^5$; the corresponding rastering velocities are (a)–(c) $\nu=0.001$ and (d) $\nu=0.0005$; in all the cases, $\Gamma_2=0.02$.

dent runs. As one would expect, the overall behavior of β_X is very similar to the behavior of β_Z for the same parameters as the binary case [Fig. 8(c)] because the origin of the ordering process is the same for both procedures. However, there are some differences between the graphs in Figs. 8(c) and 11. In particular, relative to the binary case, the plots for the ternary case exhibit larger error bars, a less smooth increase of the ordering at the early and intermediate times, and smaller absolute values of the ordering at late times. We attribute these differences to the distortions of the C region due to the moving Γ_2 region [see Figs. 10(b)–10(d)]. Since the latter distortions decay away from the moving Γ_2 region, the ordering away from these regions is high (i.e., it is higher than the saturation value in the Fig. 11). In other words, the local distortions decrease the final value of the ordering in Fig. 11.

The patterns obtained using the proposed technique are stable under the conditions imposed on the system (i.e., as long as the reaction rate coefficients are held at the specified values). With rapid quenching, for example, the systems described above can be frozen to form a solid that exhibits the morphology of the molten state.

C. Examples indicating the effect of light attenuation within sample

In the above calculations, we assumed that the absorption of light is small and can be neglected over the entire thickness of the sample. In other words, the applied light leads to a constant value of Γ_2 at each point within the sample. In the following, we show how the evolution of the ternary blends [for the geometry shown in the schematic in Fig. 9(a)] is altered in the cases where the absorption of light within the sample is explicitly taken into account. We take the following functional form for the reaction rate constants:

$$\Gamma_{1,2}(x,y,z)=\Gamma_{1,2}^{0}\exp\left(-\frac{y-\int_0^y\psi(x,y,z)dy-y_0}{R_0}\right). \tag{18}$$

Here, we assume that the light is shinning on the front side of the sample, with the $y=0$ plane in Fig. 9(a) defining what is meant by "front." The $\Gamma_{1,2}^{0}$ are the reaction rate coefficients at $y=y_0=0$ (the front) and R_0 is the distance that characterizes the light attenuation within the A and B components. We assume that the C component remains transparent; i.e., there is no attenuation of the light intensity within C. Therefore, the effective thickness of the AB material "in front of" the point (x,y,z) is taken to be $y-\int_0^y\psi(x,y,z)dy$ in Eq. (18). In other words, if only C $(\psi\approx1)$ is in front of this point, the "thickness" of the AB material is zero; if there is no C component in front of this point, the thickness of the AB material is y.

In addition, in the following simulations we modified the boundary conditions such that we now have hard walls at $y=0$ and at $y=L_y$, while we still maintain periodic boundary conditions in the x and z directions. The hard walls are assumed to be neutral, so that in addition to the condition of no material flux through the walls [i.e., $(\nabla\mu_\varphi\cdot\mathbf{n})=0$ and $(\nabla\mu_\psi\cdot\mathbf{n})=0$], we also apply $(\nabla\varphi\cdot\mathbf{n})=0$ and $(\nabla\psi\cdot\mathbf{n})=0$, where $\mathbf{n}$ is the unit vector normal to the hard wall.

Figure 12 illustrates the late-time morphology for the system shown schematically in Fig. 9(a) (with the stationary and rastering higher-intensity light), given the functional dependence of the reaction rate coefficients in Eq. (18). The image in Fig. 12(a) shows the morphology at a late time $(t=6\times10^5)$ for $R_0=3L_y$. In this case, the attenuation of the light occurs gradually over a large distance and, thus, modifications to the reaction rate coefficient are negligibly small. Figure 12(a) looks similar to Fig. 9(c), which otherwise corresponds to the same simulation time and the same system parameters. The most significant difference between Figs. 12(a) and 9(c) is caused not by the attenuation of the light intensity, but by the changes in the boundary conditions. Recall that we now have neural hard walls at $y=0$ and at $y=L_y$. These neutral walls give rise to the preferential perpendicular orientation of the AB domains at these boundaries (as can be most clearly seen on the back walls in Fig. 12).

The images in Figs. 12(b) and 12(c) show late-time morphologies for the cases where the effect of the attenuation of the light intensity becomes more important. We chose $R_0 = L_y$ and $R_0 = L_y/4$ for the cases in Figs. 12(b) and 12(c), respectively. In all the cases, the C component still migrates to the stationary Γ_2 region; however, the lower the values of R_0 (i.e., the more reaction the rate constant decreases away from the front of the sample), the wider the layer of C in the front. The C component always migrates to the regions with the higher reaction rate coefficients (as we explained above), and those regions are now in the front of the sample due to the light attenuation. In addition, the characteristic time needed for the saturation of the stationary stripe with the C component becomes larger as R_0 becomes smaller since the average reaction rate coefficient within the stationary stripe also becomes smaller.

The morphologies within the AB domains in Figs. 12(b) and 12(c) llustrate that, as one expects, the AB lamellar thickness at the back of the sample becomes larger as R_0 becomes smaller. The moving Γ_2 region introduces an ordering within the "combing" direction; however, this ordering becomes smaller as R_0 becomes smaller. This is mostly due to the fact that the average reaction rate coefficient within the moving region becomes smaller. In addition, we note that due to the mismatch between the lamellae thickness at the front and back of the sample, the three-dimensional ordering of the form shown in Fig. 10 would no longer be possible for relatively small R_0, even after the second combing step along the x direction. Rather, in this scenario, a gradient material could potentially be formed.

We also note that in additional preliminary studies, we probed effects due to the adsorption of light within the C component. In particular, we ran simulations for the cases where the light adsorption within the C component is the same as within the AB domains and we found that for the intermediate values of $R_0 \approx L_y$, the late-time morphologies are similar to the morphologies shown in Fig. 12, except for the distinctively greater widening of the C domain close to the front of the sample. Detailed studies of systems with different light adsorptions characteristics are the subject of a separate study.

D. Example relating the dimensionless simulation parameters and physical values

In the following, we give an example of the relationship between our dimensionless simulation parameters and physical dimensional values. In particular, if we equate the distance between two lattice sites to $\zeta \approx 10^{-7}$ m, then the choice of the dimensional diffusion constant D gives the time scale for one simulation time step as $\tau \approx \zeta^2 2M_\varphi a_{20}/D \approx \zeta^2 0.076/D$ (where we use the dimensionless value for the diffusion constant from our simulation, $2M_\varphi a_{20} = 0.076$). If we take the value of $D \approx 10^{-14}$ m^2/s, we find that the time step in our simulations corresponds to $\tau \approx 0.076$ s and the dimensional combing speed $v\zeta/\tau \approx 2.6 \times 10^{-9}$ m/s (where $v = 0.002$ is the dimensionless value of the combing speed). In other words, in the above example, our 3D sample can be "combed out" in $\approx 5.7 \times 10^3$ s with the smallest features being on $10\zeta \approx 1$ μm (note that the height of the sample is $150\zeta \approx 15$ μm).

In order to roughly estimate the effective length for the light intensity attenuation due to the reaction, we assume that both the forward and backward reactions consume a single photon with energy $h\gamma$ (i.e., here, we neglect the fact that the adsorption wavelengths for the forward and the backward reactions could be different, and we also neglect any interference between the two light sources [32]). Therefore, the change in the intensity of light, I, passing through the sample of thickness dy can be found as $dI = -\Gamma h\gamma N_R dy$. The concentration of the reaction centers, N_R, is defined by the molar mass of the A (B) component M_w as $N_R = N_A \rho / M_w$. Here N_A is Avogadro's number and ρ is a mass density; it is also assumed that there is a single reaction center per molecule. In addition, we assume a linear dependence between the reaction rate coefficient and the light intensity I so that $\Gamma = \alpha I$. In the estimates below, we use the following physical values: the intensity and the wavelength of the light are taken to be $I \approx 3$ mW/cm^2 and $\lambda \approx 400$ nm respectively, the mass density is $\rho \approx 1$ g/cm^3 and the molar mass of the A (B) is $M_w \approx 1.4 \times 10^4$. Finally, we find the proportionality constant α using the above value for the light intensity and the dimensional value for the reaction rate constant, $\Gamma = 0.003/\tau$ (here we take 0.003 as the dimensionless value of the reaction rate coefficient used in the simulations). Taking into account all the physical values given above, we find that the characteristic length for the light attenuation within the sample is $(\alpha h\gamma N_R)^{-1} \approx 3L_y$ (here $L_y = 120\zeta$ is the dimensional thickness of the sample). Therefore, the parameters chosen above correspond to the case shown in Fig. 12(a). We also note that by choosing higher values for the molecular weight, lower values for the diffusivity, and higher values for the characteristic length scale, one can significantly (e.g., by a couple of orders of magnitude) increase the effective characteristic length for the light attenuation within the sample; however, the latter parameters will also cause a slower evolution of the system.

IV. CONCLUSIONS

We considered ABC ternary blends where the A and B components undergo a reversible photochemical reaction, which leads to phase separation between A and B. In addition, the nonreactive C component is assumed to be immiscible with both A and B. Using computer simulations, we have shown that this ternary mixture can be ordered into regular, periodic structures by exposing the system to both spatially dependent and time-dependent light irradiation. We first focused on the effects of illuminating the system with just the spatially dependent light irradiation. Experimentally, this would correspond to using both a uniform background light and a localized, well-collimated light source. We assumed that the well-collimated light has a higher intensity than the background light. To model this scenario, we utilized a three-dimensional simulation box that contains two distinct regions, where each region is characterized by a different reaction rate coefficient. For the region illuminated by the background light, the rate coefficient is given by Γ_1, while the region illuminated by the well-collimated, higher-intensity light is characterized by a rate coefficient of $\Gamma_2 > \Gamma_1$. (Here, we assumed that the forward and reverse rate coefficients for the reversible reaction are equal.)

We found that the reactive *AB* mixture will diffuse out of the Γ_2 regions, while the nonreactive *C* component will diffuse into these regions. Thus, by directing the collimated, higher-intensity light onto selected regions, one can write a three-dimensional pattern of *C* on the *AB* reactive blend. This approach provides a noninvasive, robust means of writing with the *C* "ink" and is effective for a wide range of system parameters.

A necessary condition for successfully writing the desired *C* pattern is that the amount of *C* within the system is such that the *C* effectively fills the higher-intensity region (or regions). We derived an additional criterion that allows us to predict, for different system parameters, the sharpness of the written pattern (i.e., how closely the shape of the *C* domain replicates the geometry of the Γ_2 region). We showed that the writing is sharper for relatively high values of Γ_2 and relatively low values of the interfacial tension between the *A* (*B*) and *C* components.

We then demonstrated how moving the Γ_2 region through the 3D sample could lead to spatially ordered binary and ternary blends. In experiments, such motion would correspond to rastering over the sample with the well-collimated light source. We first showed that for a specified range of the rastering velocities, the moving, higher-intensity light "combs out" defects within the *AB* lamellar domains and the system becomes ordered along the combing direction. This ordering occurs because the moving Γ_2 region creates a moving "neutral" boundary, which drives the reorientation of the *AB* domains perpendicular to this interface (that is, along the rastering direction). The results also reveal that the binary blend can be ordered in all three directions by applying the proposed technique twice—i.e., by rastering the higher-intensity light along *z* and then along *x*.

By combining the two effects described above (the migration of *C* to stationary Γ_2 domains and the combing of the *AB* domains with the moving Γ_2 regions), one can create a variety of defect-free, hierarchically ordered multicomponent materials. For example, one can create defect-free materials that exhibit a periodicity over two distinct length scales, where one length scale is defined by the thickness of the *AB* lamellae and the second length scale is defined by the size of the *C*-filled stationary Γ_2 regions. Since our approach involves homopolymers, it significantly expands the range of materials that can be fashioned into a periodic pattern and could potentially provide advantages over current photolithographic techniques since the proposed process is fully reversible, noninvasive, and points to a novel means of writing patterns in three dimensions.

ACKNOWLEDGMENTS

The authors gratefully acknowledge discussions with Professor Mary Galvin and Professor Tom Russell. This work was supported by the DOE. Partial support for some of the work was provided by NSF to O.K. and ARO to R.D.M.T.

APPENDIX

At each time step, we update the value of each order parameter according to the following rules:

$$\varphi(\mathbf{r},t+1) = \varphi(\mathbf{r},t) + \tilde{M}_\varphi[\langle\langle\tilde{\mu}_\varphi(\mathbf{r},t)\rangle\rangle - \tilde{\mu}_\varphi(\mathbf{r},t)] - 2\Gamma(\mathbf{r},t)\varphi(\mathbf{r},t), \tag{A1}$$

$$\psi(\mathbf{r},t+1) = \psi(\mathbf{r},t) + \tilde{M}_\psi[\langle\langle\tilde{\mu}_\psi(\mathbf{r},t)\rangle\rangle - \tilde{\mu}_\psi(\mathbf{r},t)]. \tag{A2}$$

Here, $\langle\langle * \rangle\rangle - *$ is the isotropic discrete Laplacian on a cubic lattice, with $\langle\langle * \rangle\rangle$ taken as [33]

$$\langle\langle * \rangle\rangle = \frac{6}{80}\sum_{\mathrm{NN}} * + \frac{3}{80}\sum_{\mathrm{NNN}} * + \frac{1}{80}\sum_{\mathrm{NNNN}} * , \tag{A3}$$

where {NN}, {NNN}, and {NNNN} denote summation over the nearest, next-nearest, and next-next-nearest neighbors, correspondingly. We note that there is a proportionality constant *c* between the above form of the isotropic discrete Laplacian and the Laplacian in the continuum equations (2) and (3) [33,34]:

$$\langle\langle * \rangle\rangle - * = c\nabla^2 * . \tag{A4}$$

With the averaging in Eq. (A3), this proportionality constant is $c = 11/40$ [33]; this constant has to be taken into account to define an accurate correspondence between the appropriate CDS scheme and continuum equations. The $\tilde{\mu}_\varphi(\mathbf{r},t)$ and $\tilde{\mu}_\psi(\mathbf{r},t)$ are related to the chemical potentials defined in Eq. (4) and are updated according the following rules:

$$\tilde{\mu}_\varphi(\mathbf{r},t) = \tilde{f}_\varphi(\varphi(\mathbf{r},t),\psi(\mathbf{r},t)) - \tilde{D}_\varphi[\langle\langle\varphi(\mathbf{r},t)\rangle\rangle - \varphi(\mathbf{r},t)], \tag{A5}$$

$$\tilde{\mu}_\psi(\mathbf{r},t) = \tilde{f}_\psi(\psi(\mathbf{r},t),\psi(\mathbf{r},t)) - \tilde{D}_\psi[\langle\langle\psi(\mathbf{r},t)\rangle\rangle - \psi(\mathbf{r},t)], \tag{A6}$$

where

$$\tilde{f}_\varphi(\varphi(\mathbf{r},t),\psi(\mathbf{r},t)) = \varphi(\mathbf{r},t) - A\tanh\varphi(\mathbf{r},t) + 2ca_{22}\varphi(\mathbf{r},t)\psi^2(\mathbf{r},t), \tag{A7}$$

$$\tilde{f}_\psi(\varphi(\mathbf{r},t),\psi(\mathbf{r},t)) = c[2a_{02}\psi(\mathbf{r},t) + 2a_{22}\varphi^2(\mathbf{r},t)\psi(\mathbf{r},t) - 3a_{03}\psi^2(\mathbf{r},t) + 4a_{04}\psi^3(\mathbf{r},t)]. \tag{A8}$$

If there is no *C* in the system $[\psi(\mathbf{r},t)=0]$, the above model reduces to the standard CDS model for a binary fluid, where the map $\varphi(\mathbf{r},t) - A\tanh\varphi(\mathbf{r},t)$ is chosen [26,33]. In the above simulations, we set $A=1.31$, $\tilde{D}_\varphi=0.5$, $\tilde{D}_\psi=1.5$, $\tilde{M}_\varphi=1$, and $\tilde{M}_\psi=1/3$. We note that $\varphi(\mathbf{r},t) - A\tanh\varphi(\mathbf{r},t) \approx c[-\varphi(\mathbf{r},t)+\varphi(\mathbf{r},t)^3]$ for $\varphi(\mathbf{r},t)\in[-1;1]$ and $c=11/40$; therefore, the relationship between the chemical potentials defined in Eq. (4) and the definitions in Eqs. (A5) and (A6) is $\tilde{\mu}_\varphi \approx c\mu_\varphi$ and $\tilde{\mu}_\psi \approx c\mu_\psi$ with $\kappa_\varphi = \tilde{D}_\varphi/2$ and $\kappa_\psi = \tilde{D}_\psi/2$, and the relationship between the mobilities in Eqs. (2) and (3) and the CDS values in Eqs. (A1) and (A2) is $M_\varphi = c^2 \widetilde{M}_\varphi$ and $M_\psi = c^2 \widetilde{M}_\psi$. We also note that while the above expansion $c[-\varphi(\mathbf{r},t)+\varphi(\mathbf{r},t)^3]$ is a good approximation for the $\varphi(\mathbf{r},t) - A \tanh \varphi(\mathbf{r},t)$ on the whole interval of the values of the order parameter $\varphi(\mathbf{r},t) \in [-1;1]$, for small values of $\varphi(\mathbf{r},t) \ll 1$, the Taylor expansion around $\varphi(\mathbf{r},t)=0$ gives $\varphi(\mathbf{r},t) - A \tanh \varphi(\mathbf{r},t) \approx c[-1.14\varphi(\mathbf{r},t)+1.59\varphi(\mathbf{r},t)^3]$ and therefore $\widetilde{a}_{20}=0.569$ and $\widetilde{a}_{40}=0.398$.

---

[1] L. Rockford, S. G. J. Mochrie, and T. P. Russell, Macromolecules **34**, 1487 (2001).

[2] M. P. Stoykovich *et al.*, Science **308**, 1442 (2005), S. O. Kim *et al.*, Nature (London) **424**, 411 (2003); E. W. Edwards *et al.*, Adv. Mater. (Weinheim, Ger.) **16**, 1315 (2004).

[3] R. D. M. Travasso, O. Kuksenok, and A. C. Balazs, Langmuir **21**, 10912 (2005).

[4] R. D. M. Travasso, O. Kuksenok, and A. C. Balazs, Langmuir **22**, 2620 (2006).

[5] Q. Tran-Cong, J. Kawai, and K. Endoh, Chaos **9**, 298 (1999).

[6] H. Nishioka, K. Kida, O. Yano, and Q. Tran-Cong, Macromolecules **33**, 4301 (2000); H. Nakanishi, M. Satoh, T. Norisuye, and Q. Tran-Cong-Miyata, *ibid.* **37**, 8495 (2004) and references therein.

[7] Q. Tran-Cong-Miyata, S. Nishigami, T. Ito, S. Komatsu, and T. Norisuye, Nat. Mater. **3**, 448 (2004).

[8] S. C. Glotzer, D. Stauffer, and N. Jan, Phys. Rev. Lett. **72**, 4109 (1994).

[9] S. C. Glotzer, E. A. Di Marzio, and M. Muthukumar, Phys. Rev. Lett. **74**, 2034 (1995).

[10] S. Puri and H. L. Frisch, J. Phys. A **27**, 6027 (1994).

[11] J. J. Christensen, K. Elder, and H. C. Fogedby, Phys. Rev. E **54**, R2212 (1996).

[12] C. Huang, M. Olvera de la Cruz, and B. W. Swift, Macromolecules **28**, 7996 (1995).

[13] C. Huang and M. Olvera de la Cruz, Phys. Rev. E **53**, 812 (1996).

[14] K. Tafa, S. Puri, and D. Kumar, Phys. Rev. E **64**, 056139 (2001).

[15] Y. Ma, J. Chem. Phys. **114**, 3734 (2001).

[16] S. Puri and D. Kumar, Phys. Rev. E **70**, 051501 (2004).

[17] R. D. M. Travasso *et al.*, J. Chem. Phys. **122**, 194906 (2005).

[18] K. C. Lakshmi and P. B. Sunil Kumar, Phys. Rev. E **67**, 011507 (2003).

[19] C. Tong and Y. Yang, J. Chem. Phys. **116**, 1519 (2002).

[20] T. Okuzono and T. Ohta, Phys. Rev. E **67**, 056211 (2003).

[21] K. Good *et al.*, J. Chem. Phys. **121**, 6052 (2004).

[22] Y. J. Zhu and Y. Q. Ma, Phys. Rev. E **67**, 021804 (2003).

[23] B. Liu, C. H. Tong, and Y. L. Yang, J. Phys. Chem. **105**, 10091 (2001).

[24] T. Ohta and A. Ito, Phys. Rev. E **52**, 5250 (1995).

[25] Here, we assume that the viscosity of the mixture is sufficiently high that hydrodynamics effects do not play a role in the system's behavior [see A. J. Bray, Adv. Phys. **43**, 357 (1994)]; hence, we neglect hydrodynamic effects in the system of equations (2) and (3).

[26] Y. Oono and S. Puri, Phys. Rev. A **38**, 434 (1988).

[27] F. Liu and N. Goldenfeld, Phys. Rev. A **39**, 4805 (1989).

[28] M. Bahiana and Y. Oono, Phys. Rev. A **41**, 6763 (1990).

[29] It is also well known that in such binary reactive systems, one can observe morphologies that resemble not only lamellae, but also the hexagonal patterns of asymmetric diblocks if the rates coefficients of the forward and reverse reactions in Eq. (1) are not equal (see, for example, [9]).

[30] P. G. de Gennes, Rev. Mod. Phys. **57**, 827 (1985).

[31] G. J. Kellogg, D. G. Walton, A. M. Mayes, P. Lambooy, T. P. Russell, P. D. Gallaghev, and S. K. Satija, Phys. Rev. Lett. **76**, 2503 (1996).

[32] Even for cases of reactive blends where the adsorption wavelengths for the forward and backward reactions are significantly different, we expect that the overall behavior of the system (i. e., the writing and the ordering processes) will remain the same, as long as both wavelengths are included in both the rastering and background light beams.

[33] A. Shinozaki and Y. Oono, Phys. Rev. E **48**, 2622 (1993).

[34] Y. Oono, Phys. Rev. E **55**, 3792 (1997).